Title:

Interior near-field acoustic holography based on finite elements

Running title:

Near-field acoustic holography with finite elements

Name: Steffen Ungnad

Postal address: Department of Mechatronics, Helmut Schmidt University, Holstenhofweg 85, 22043 Hamburg, Germany

E-mail address: ungnads@hsu-hh.de

Telephone: +49 40 6541 3723

Name: Delf Sachau

Postal address: Department of Mechatronics, Helmut Schmidt University, Holstenhofweg 85, 22043 Hamburg, Germany

E-mail address: sachau@hsu-hh.de

Telephone: +49 40 6541 2733

Abstract

This paper deals with the mathematical framework of near-field acoustic holography based on finite elements in application to the acoustic response of a fluid within a closed cavity to the enclosure boundary conditions. The finite element method is an effective implementation of the modal approach for arbitrary geometries and provides advantages for certain wavenumber intervals in rooms. An inverse implementation of the direct problem can benefit from using generalized coordinates with modally reduced system matrices. A solution can be obtained via singular value decomposition together with Tikhonov regularization. This paper investigates acoustic mode spectrums of acoustic transfer functions, which has a major effect on the reconstruction of particle velocities from given sound pressures in a simple cavity model. It is found that the largest considered modal wavenumber in the acoustic transfer matrix should be twice the maximum excitation wavenumber. Furthermore, the relation between reconstruction errors and the detectability of evanescent waves depending on the wavenumber of excitation is considered. The proposed method is validated experimentally by reconstructing particle velocities on the inner boundaries of an Airbus A400M fuselage based on measurements of the inner pressure field. Results are compared with structural velocities measured with a laser Doppler vibrometer.

I. INTRODUCTION

One of the tasks of an acoustic engineer is to eliminate noise by studying the dominance of interior sound sources. Requirements such as finite time resources and large regions that are inaccessible for measurement lead to the approach of model-based inverse source problems. However, which inverse technique to use depends strongly on the direct problem formulation and the acoustic environment, and it is well known that there is no optimum way to locate the sources of noise. One can choose from a broad range of acoustic source reconstruction tools, and the need remains for high-resolution methods for localizing sound sources in interior domains. A wide variety of inverse methods can be derived from direct acoustic problem formulations.

Near-field acoustic holography[1] (NAH) and its subsequent statistically optimized complement[2] originate from Fourier optics[3] and have led to a breakthrough in the field of applied inverse problems in acoustics. Those methods involve measuring on a hologram plane close to a radiating structure to capture evanescent waves and to reconstruct acoustic quantities in the source plane with a resolution of less than half an acoustic wavelength. The input data can be either the sound pressure or its gradient.[4] The violation of the inherent free-field assumption due to reflection in the context of Fourier-based NAH can be tackled through field separation techniques[5,6] or by using simple geometries with well-defined boundary conditions.[7] The pressure fields of volumes with irregular geometry can be calculated using numerical methods such as the boundary element method (BEM),[8] which is especially useful for free-field applications because its formulation meets the Sommerfeld radiation condition. Moreover, it is used widely for inverse localization of interior sound sources.[9–11] The disadvantages of BEM are (i) having to integrate over a singular kernel and (ii) the computational load needed to generate frequency-dependent fully populated acoustic transfer matrices.

Another approach results from the ability to predict acoustic sound radiation using spherical sources with application to the free field[12,13] and enclosed sound fields.[14,15] Reversing this approach leads to methods such as the Helmholtz-equation least-squares method[16] or the equivalent-source method (ESM-based NAH) for reconstructing interior sound fields.[17,10] However, ESM-based NAH results in a complicated optimization problem: not only the source strength but also the number and position of the elementary sources and receivers must be determined, and the solutions depend strongly on the geometry as well as on the wavelength, an issue that persists regarding source localization.[18–20] Another way of source localization is to directly measure and invert the transfer function between sources and receivers,[21,22] although achieving high resolution requires considerable measurement effort.

Inverse source formulations are mathematically linear ill-posed problems, therefore direct or iterative regularization can alleviate the implied errors.[23] Tikhonov regularization is a direct method with wide application for solving inverse problems.[24] However, because it is not easy to choose the regularization parameter,[25,26] methods for doing so always involve an approximation in the form of a trade-off between over-smoothing and error amplification.[27]

With precise information about interior Green's functions satisfying Neumann or Dirichlet boundary conditions, an equivalent solution to the Kirchhoff integral equation used in BEM-based NAH can be found.[28] This procedure is called the modal approach[29] or the Green's function method,[30] and it is usually applied to problems with well-separated acoustic modes[31] where the ratio of the cavity dimensions to the acoustic wavelength is less than three.[32] However, the classical modal approach is not feasible for arbitrary geometries, and alternative methods are required. Wave-based computational methods such as the finite difference method[33] or the finite element method[34] (FEM) are used widely to solve direct problem formulations in arbitrary acoustic

domains. However, inverse sound source localization based on the modal approach remains limited to geometries for which the wave equation is separable.[35]

The aim of the first inverse field problems solved with finite elements was to reconstruct a complete pressure field using just a few microphones in a cavity.[36,37] Another approach minimized the acoustic potential energy in a discretized cavity to identify the dominant sound sources.[38] However, doing so leads to matrices of impractical size for which iterative inversion is mandatory. Furthermore, in computational examples in which finite elements were used to approximate an acoustic free field, the sound sources were found effectively by fitting parameters of a sparsity promoting Tikhonov functional.[39] Because large finite element models entail many degrees of freedom, an eigenvalue problem with modally reduced matrices can be solved instead to describe the system properties.[40] Therefore, an inverse approach arises from impedance-based sub-structuring techniques,[41,42] and it uses the approximation of the acoustic modes of a sub-cavity to reconstruct local sources based on mixed or uniform boundary conditions. However, because these modes are non-physical ones, many sound pressure measurements or measurements of sound pressure gradients on surrounding virtual surfaces are required. Furthermore, the dimensions of the virtual sub-cavities are restricted by the measurement distance when capturing evanescent waves. Other FEM-based approaches attempt to reconstruct iteratively the boundary admittance in arbitrarily shaped volumes using a reduced matrix formulation based on the Robin boundary condition.[43] The main concern here is to determine the boundary admittance assuming a given excitation. This leads to another family of methods aimed at reconstructing the boundary admittance directly either by using BEM[44] or by iteratively updating a finite element model based on sensitivity functions.[45,46]

The motivation behind the intended formulation of FEM-based NAH is to use the advantages of the numerical modal approach for interior sound fields to inversely reconstruct acoustic sources

resulting from structural vibrations. In the proposed approach, sound pressure measurements in a cavity are related to the normal particle velocities on the cavity boundary by a linear approximation of the acoustic environment with finite elements. Because there are several FEM software packages, this approach may equip a wider range of practitioners with methods for localizing sound sources. The proposed procedure is from the same FEM-based family as the sub-structuring approach but avoids having to measure sound pressures or particle velocities on virtual boundary surfaces.

This paper is organized as follows. Section II describes the theory behind extracting an acoustic transfer function from a finite element model. In Section III, the application of the modal approach to a simple two-dimensional (2D) cavity model covers the main aspects of the inverse solution in FEM-based NAH. Section IV provides experimental results obtained from the cavity of a full-scale Airbus A400M fuselage. Finally, conclusions are drawn in Section V.

II. MATHEMATICAL FORMULATION

A. Modal approach methodology

The model depicted in FIG. 1 represents a harmonic sound field in an arbitrarily shaped volume V enclosed by a boundary Π with $\mathbf{r}_b \in \mathbb{R}^{3\times1}$ (with time dependence $e^{-j\omega t}$), where ω is the acoustic angular frequency and j is the imaginary unit ($j^2 = -1$). Calculation of the steady-state sound pressure p at points of observation $\mathbf{r}_m \in \mathbb{R}^{3\times1}$ in the measurement domain Ω is possible using Green's second identity applied to acoustic quantities:[47]

$$p(\mathbf{r}_m) = \oint G(\mathbf{r}_m|\mathbf{r}_b)\frac{\partial p}{\partial \mathbf{n}}(\mathbf{r}_b)\, d\mathbf{r}_b - \oint \frac{\partial G(\mathbf{r}_m|\mathbf{r}_b)}{\partial \mathbf{n}}p(\mathbf{r}_b)d\mathbf{r}_b, \qquad (1)$$

6

which is a representation of the sound pressure at any field point in Ω as an integral involving the sound pressure and its surface gradient on Π. The measurement domain is source free and does not coincide with the boundary.
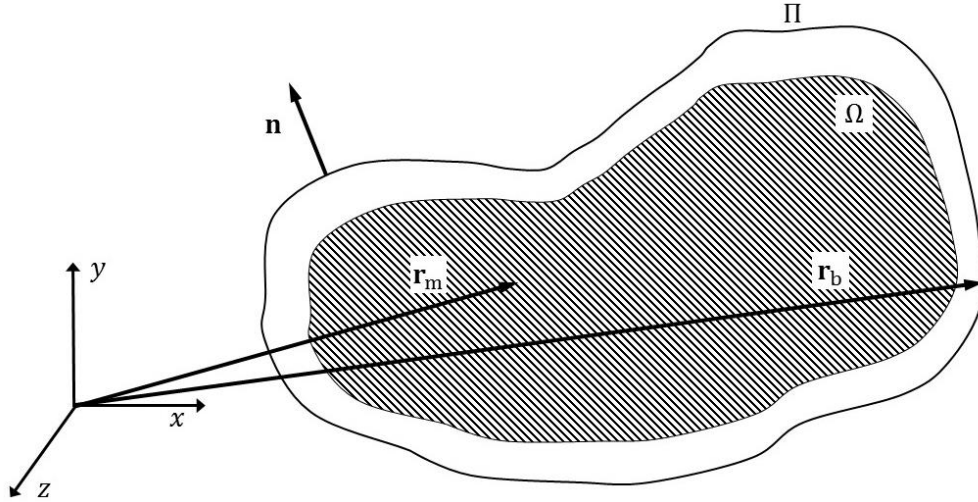

FIG. 1. Geometric definition of an interior measurement region Ω bounded by the surface Π. Note that the normal vector **n** is directed outward.

The direct BEM inserts the general expression of the free-space Green's function for a harmonic point monopole into Eq. (1) to express the pressure field in terms of a monopole and dipole source distribution on the surrounding surface. By contrast, the modal solution has a well-defined boundary condition to eliminate one term in Eq. (1). Commonly, a vanishing surface gradient is used (Neumann boundary condition):

$$\frac{\partial G(\mathbf{r}_\mathrm{m}|\mathbf{r}_\mathrm{b})}{\partial \mathbf{n}} = 0, \tag{2}$$

which represents a homogeneous equilibrium relationship with the normal particle velocity specified on the boundary. The sound pressure surface gradient is replaced by Euler's equation:

$$-\frac{\partial p}{\partial \mathbf{n}}(\mathbf{r}_\mathrm{b}) = \mathrm{j}\omega\varrho v(\mathbf{r}_\mathrm{b}), \tag{3}$$

which leads to a Fredholm integral equation of the first kind:

$$p(\mathbf{r_m}) = -j\omega\varrho \oint G_N(\mathbf{r_m}|\mathbf{r_b})v(\mathbf{r_b})d\mathbf{r_b}, \tag{4}$$

where ϱ is the density of the fluid. With this, one tries to construct a Green's function to express the solution of the boundary value problem as an integral of the product of a kernel function and the known normal particle velocity on the boundary. The Neumann Green's function $G_N(\mathbf{r_m}|\mathbf{r_b})$ represents the integral kernel and $v(\mathbf{r_b})$ encompasses the complex excitation function that superimposes the surface motion $v_s(\mathbf{r_b})$ of the surrounding structure with the particle motion as the result of an arbitrary local boundary admittance $Y(\mathbf{r_b})$. To take both quantities into account, a mixed boundary condition is proposed, namely[48,49]

$$v(\mathbf{r_b}) = v_s(\mathbf{r_b}) + Y(\mathbf{r_b})p(\mathbf{r_b}). \tag{5}$$

Note that $Y(\mathbf{r_b})$ depends on the wave angles of incidence. The required Green's function must satisfy the inhomogeneous Helmholtz equation

$$(\Delta + k^2)G_N(\mathbf{r_m}|\mathbf{r_b}) = -\delta(\mathbf{r} - \mathbf{r_b}), \tag{6}$$

which relates the three-dimensional (3D) Dirac delta function $\delta(\mathbf{r} - \mathbf{r}_b)$ at the origin on the boundary Π to the sound pressure at any field point in the volume Ω. Here, k is the acoustic angular wavenumber. In the modal contribution theory, Green's functions $G_N(\mathbf{r_m}|\mathbf{r_b})$ can be expanded as a series of E solutions in terms of eigenfunctions:[29]

$$G_N(\mathbf{r_m}|\mathbf{r_b}) = \sum_{n=1}^{E} \frac{1}{\iiint \varphi_n(\mathbf{r_m})^2 d\mathbf{r_m}} \frac{\varphi_n(\mathbf{r_m})\varphi_n(\mathbf{r_b})}{(k_n^2 - k^2)}. \tag{7}$$

The eigenvalues are in ascending order $0 \leq k_1 \leq k_2 \leq \cdots \leq k_n$, with the eigenfunctions φ_n creating a complete set of orthogonal functions that satisfy the first-order homogeneous boundary condition in Eq. (2). This characteristic functions are known as uncoupled rigid-wall modes with their corresponding resonance wavenumbers k_n. By substituting Eq. (7) into Eq. (4), the given

excitation function $v(\mathbf{r}_b)$ can be integrated over Π. Consequently, this leads to the linear mapping of the sound field from Π to Ω through an impedance term:

$$p(\mathbf{r}_m) = -\mathrm{j}\omega\varrho \sum_{n=1}^{E} \frac{\varphi_n(\mathbf{r}_m)}{\iiint \varphi_n(\mathbf{r}_m)^2 d\mathbf{r}_m} \frac{1}{(k_n^2 - k^2)} \oint \varphi_n(\mathbf{r}_b)v(\mathbf{r}_b)\, d\mathbf{r}_b. \qquad (8)$$

This represents the direct problem formulation with Neumann boundary conditions, where a pressure field $p(\mathbf{r}_m)$ is determined uniquely by the velocity boundary condition $v(\mathbf{r}_b)$. The first term in Eq. (8) incorporates an undamped acoustic mode normalized by a shape-specific factor. According to the following resonance denominator, the influence of a mode grows if the wavenumber k is close to the mode eigenvalue k_n. This leads to a decay of modal excitation amplitudes away from the radiation circle in inverse proportion to the difference of the squared wavenumbers. The third term in Eq. (8) grows if the phase velocities $v(\mathbf{r}_b)$ of the excitation function and an acoustic mode $\varphi_n(\mathbf{r}_b)$ overlap. It also accounts for dissipative boundary segments leading to modal coupling by their equivalent pressure field in Eq. (5). Furthermore, this term describes the evanescence triggered by inhomogeneous wave components outside the radiation circle. Although these waves do not play a critical role in forward mapping, they are crucial for backward projection.

B. Inverse problem for modal approach

In backward projection, $v(\mathbf{r}_b)$ in Eq. (8) is replaced by the Dirac delta function $\delta(\mathbf{r} - \mathbf{r}_b)$. With the sifting property, one obtains the impedance

$$Z(\mathbf{r}_m|\mathbf{r}_b) = -\mathrm{j}\omega\varrho \sum_{n=1}^{E} \frac{\varphi_n(\mathbf{r}_m)\varphi_n(\mathbf{r}_b)}{\iiint \varphi_n(\mathbf{r}_m)^2 d\mathbf{r}_m} \frac{1}{(k_n^2 - k^2)}. \qquad (9)$$

Discrete sampling generates the standard form used to reconstruct the particle velocities $\mathbf{v} \in \mathbb{C}^{B \times 1}$ at boundaries based on sound pressures $\mathbf{p} \in \mathbb{C}^{M \times 1}$ given by[50]

$$\mathbf{p} = \mathbf{Z}\mathbf{v}. \tag{10}$$

This expression relates the B unknown particle velocities on Π to the M known sound pressures in the hologram domain Ω. Inverting the rectangular acoustic transfer matrix $\mathbf{Z} \in \mathbb{C}^{M \times B}$ is an ill-posed problem because unavoidable measurement and rounding errors occur in interaction with discrete sampling and evanescent-like waves. Thus, the compact singular value decomposition (SVD) generates an orthogonal projection for the matrix $\mathbf{Z}$ with rank R, which is given by

$$\mathbf{Z} = \mathbf{U}\boldsymbol{\Sigma}\mathbf{V}^H. \tag{11}$$

The columns of the unitary matrices $\mathbf{U} \in \mathbb{C}^{M \times R}$ and $\mathbf{V}^H \in \mathbb{C}^{R \times B}$ contain orthonormal basis vectors (singular modes). Superscript H denotes the Hermitian transpose. Small perturbations in $\mathbf{p}$ can be heavily amplified by the inverse of Eq. (11), depending on the decay properties of the singular values on the main diagonal of $\boldsymbol{\Sigma} \in \mathbb{R}^{R \times R}$. Tikhonov regularization defines a regularized pseudoinverse and leads to the solution $\tilde{\mathbf{v}} \in \mathbb{C}^{B \times 1}$ by smoothing the perturbation effects due to the reciprocal of small singular values. Therefore, the regularization parameter μ generates a trade-off between error amplification and over-smoothing for the overdetermined system of linear equations

$$\tilde{\mathbf{v}} = \mathbf{V}(\boldsymbol{\Sigma}^T\boldsymbol{\Sigma} + \mu^2\mathbf{I})^{-1}\boldsymbol{\Sigma}^T\mathbf{U}^H\mathbf{p}, \tag{12}$$

where $\mathbf{I} \in \mathbb{R}^{R \times R}$ is the identity matrix. For reproducible regularization, one can obtain the optimal value of parameter μ^o using the minimization of the mean-square errors between the given excitation and the inversely calculated particle velocities:

$$\mu^o = \min_{\mu} \frac{\|\mathbf{v} - \tilde{\mathbf{v}}(\mu)\|_2}{\|\mathbf{v}\|_2}. \tag{13}$$

In NAH-based sound-field reconstruction, to identify the sinks and sources of the sound, there is no need to deduce what fraction of the particle motion in $\tilde{\mathbf{v}}$ is induced by the structural velocity and what fraction is induced by the admittance regarding Eq. (5). Nevertheless, applying Eq. (13) requires knowledge about the boundary condition connected to the sound pressure in the hologram

plane. While that information might be available in simulations, it is not available in experiments due to the finite measurement precision. In situations in which the vibrating surface is a smooth one, the structural velocity dominates the particle motion, particularly in highly reverberant cavities subjected to structural vibration. In such cases, measurements with a laser Doppler vibrometer (LDV) lead to good approximations of the normal particle velocity at the fluid–structure interface.

C. FEM-based NAH

For an irregularly formed cavity of volume $\bar{V}$ with D degrees of freedom, nodal coordinates $\bar{\mathbf{r}} \in \mathbb{R}^{3 \times 1}$, and negligible damping, the FEM relates the unknown sound pressures $\bar{\mathbf{p}} \in \mathbb{C}^{D \times 1}$ with the given excitation $\bar{\mathbf{q}} \in \mathbb{C}^{D \times 1}$. They are connected through the assembled stiffness matrix $\mathbf{K} \in \mathbb{R}^{D \times D}$ and mass matrix $\mathbf{M} \in \mathbb{R}^{D \times D}$ with entries k_{ij} and m_{ij} as

$$k_{ij} = c^2 \int_{\bar{V}} \nabla N(\bar{\mathbf{r}})_i \nabla N(\bar{\mathbf{r}})_j d\bar{V} \tag{14}$$

and

$$m_{ij} = \int_{\bar{V}} N(\bar{\mathbf{r}})_i N(\bar{\mathbf{r}})_j d\bar{V}, \tag{15}$$

where $N(\bar{\mathbf{r}})$ is a nodal shape function using finite element discretization and c is the speed of sound. No fluid–structure interaction is considered. From the standard FEM literature, we have[33]

$$(\mathbf{K} - \mathbf{M}\omega^2)\bar{\mathbf{p}} = -\mathrm{j}\omega\varrho c^2 \bar{\mathbf{q}}. \tag{16}$$

In the case of a point source with source strength $q(\bar{\mathbf{r}})$, the load vector $\bar{\mathbf{q}}$ with entries $\bar{q}_i$ connected to nodal coordinates $\bar{\mathbf{r}}_\mathrm{b}$ becomes

$$\bar{q}_i = \int_{\bar{V}} N(\bar{\mathbf{r}})_i q(\bar{\mathbf{r}}) \delta(\bar{\mathbf{r}} - \bar{\mathbf{r}}_\mathrm{b}) d\bar{V}. \tag{17}$$

The main advantage of this approach is that it can be reformulated on a more efficient modal basis with generalized coordinates. To keep things simple, no damping matrix is taken into account. The formulation is in conjunction with Eq. (8), where the excitation term also comprises any damping caused by a normal boundary admittance. According to Bathe,[40] the vector of unknown sound pressures transforms to

$$\bar{\mathbf{p}} = \mathbf{\Psi}\boldsymbol{\eta}, \tag{18}$$

with the projection matrix $\mathbf{\Psi} \in \mathbb{R}^{D \times E}$ and unknown generalized sound pressures $\boldsymbol{\eta} \in \mathbb{C}^{E \times 1}$. Substituting Eq. (18) into Eq. (16) yields

$$(\mathbf{K} - \mathbf{M}\omega^2)\mathbf{\Psi}\boldsymbol{\eta} = -\mathrm{j}\omega\varrho c^2\bar{\mathbf{q}}. \tag{19}$$

Note that the number of degrees of freedom limits the number of columns (eigenvectors) in the projection matrix ($E \leq D$). The solution of the eigenvalue problem

$$\mathbf{K}\mathbf{\Psi} = \mathbf{M}\mathbf{\Psi}\mathbf{\Omega}^2 \tag{20}$$

delivers the **M-**orthonormal projection matrix $\mathbf{\Psi}$ and the angular eigenfrequencies $\bar{\omega}_n$, which are on the main diagonal of $\mathbf{\Omega} \in \mathbb{R}^{E \times E}$. The orthogonality relationship for the normalized eigenvectors can be written as

$$\mathbf{\Psi}^T\mathbf{M}\mathbf{\Psi} = \mathbf{I} \tag{21}$$

and

$$\mathbf{\Psi}^T\mathbf{K}\mathbf{\Psi} = \mathbf{\Omega}^2. \tag{22}$$

The identity matrix $\mathbf{I}$ and $\mathbf{\Omega}$ have the same size. Pre-multiplying by $\mathbf{\Psi}^T$ in Eq. (19) leads to

$$\mathbf{\Psi}^T(\mathbf{K} - \mathbf{M}\omega^2)\mathbf{\Psi}\boldsymbol{\eta} = -\mathrm{j}\omega\varrho c^2\mathbf{\Psi}^T\bar{\mathbf{q}}. \tag{23}$$

With Eqs. (21) and (22), this form can be rewritten as

$$(\mathbf{\Omega}^2 - \mathbf{I}\omega^2)\boldsymbol{\eta} = -\mathrm{j}\omega\varrho c^2\mathbf{\Psi}^T\bar{\mathbf{q}}. \tag{24}$$

Pre-multiplying by $(\mathbf{\Omega}^2 - \mathbf{I}\omega^2)^{-1}$ and $\mathbf{\Psi}$ together with Eq. (18) gives

$$\overline{\mathbf{p}} = -\mathrm{j}\omega\varrho c^2 \mathbf{\Psi}(\mathbf{\Omega}^2 - \mathbf{I}\omega^2)^{-1}\mathbf{\Psi}^T\overline{\mathbf{q}}. \tag{25}$$

This result is equivalent to the receptance matrix in structural mechanics with damping neglected.[51] Treating q in Eq. (17) as a unit load leads to a discrete version of the impedance function in Eq. (9) with rigid-wall eigenvalues $\overline{k}_n$ resulting from the above FEM formulation:

$$\overline{\mathbf{Z}} = -\mathrm{j}\omega\varrho \sum_{n=1}^{E} \frac{\widehat{\mathbf{\Psi}}_n \breve{\mathbf{\Psi}}_n^T}{\left(\overline{k}_n^2 - k^2\right)}. \tag{26}$$

The projection vector $\mathbf{\psi}_n \in \mathbb{R}^{D\times1}$ approximates the nth equivalent normalized eigenvector from Eq. (7) and represents the Eth column of $\mathbf{\Psi}$. Choosing the M measurement nodes and the B boundary nodes of the finite element mesh in the projection vector $\mathbf{\psi}_n$ produces $\widehat{\mathbf{\psi}}_n \in \mathbb{R}^{M\times1}$ and $\breve{\mathbf{\psi}}_n^T \in \mathbb{R}^{1\times B}$. From here, the procedure according to Eqs. (10)–(12) can be adapted to solve the system of linear equations in Eq. (25).

III. NUMERICAL EXAMPLE

The model in FIG. 2 separates the effects of evanescent-like waves from the influence of modal wavenumber spectra on a discrete inverse acoustic interior-source problem. Particular attention is paid to the backward projection of the sound field in Cartesian coordinates onto the boundary of a simple room model. This room is a rectangular parallelepiped with sides a and b. It has acoustically rigid walls in the x and y directions and is infinite in the z direction (the z coordinate is omitted). In the computer implementation, the model is sampled spatially with a square patch of size of $h = \pi/30k$. So that the ratio of the wavelength to the cavity dimension does not exceed three, the edge lengths are chosen with $ka/2\pi = 2.9$ and $kb/2\pi = 1.1$. Input sound pressures for the backward projection are evaluated in Ω for a distance of $d = 10h$ from the boundary Π. The acoustic excitation is applied in terms of an inhomogeneous Neumann boundary condition on the bottom $(y = 0)$, namely

$$v(x) = e^{-jk_{\mathrm{e}}x}.$$
(27)

The excitation wavenumber k_{e} is defined in the range from zero to $4k$ and is shown in FIG. 3 as a point moving along the k_x axis.
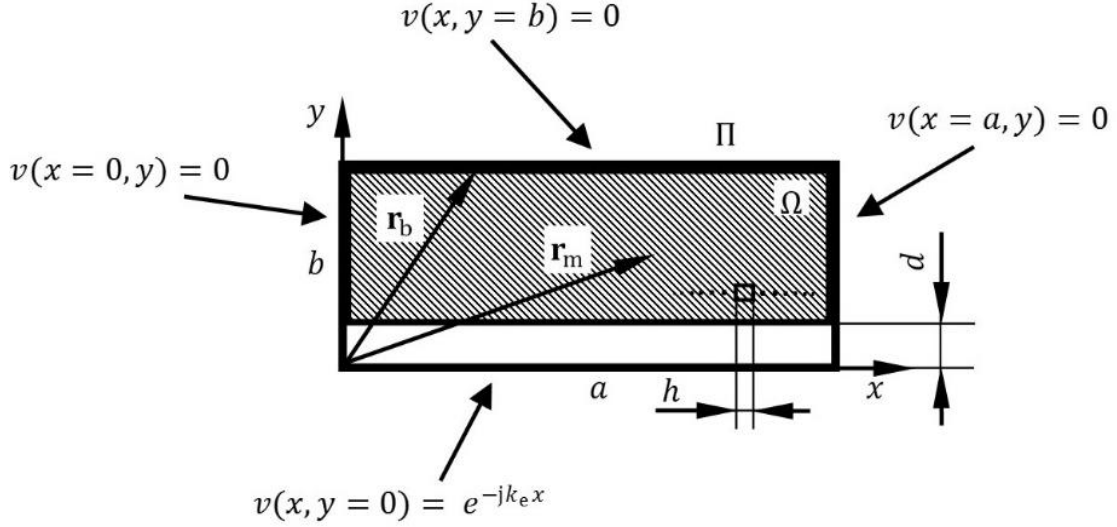

FIG. 2. Analytical room model with sides a and b in the $x - y$ plane for the inverse modal approach with a gap d between the measurement region Ω and the boundary Π. Both domains are sampled with resolution h of one sixtieth of the acoustic wavelength. An inhomogeneous Neumann boundary condition is applied to the bottom boundary at $y = 0$.

Because the eigenvalues and eigenfunctions are known,[32] the projection from the acoustic excitation on Π to the pressure field in Ω is formulated according to Eq. (8). Integration over Π leads to a sum of a resonance term multiplied by an excitation term. The first depends on the cavity dimensions and the second grows in an alternating manner if the excitation and the axial modal wavenumber coincide:

$$p(x,y) = -\frac{\omega\varrho}{ab}\sum_{r=0}^{\infty}\sum_{s=0}^{\infty}\frac{\varepsilon_r\varepsilon_s\cos(k_rx)\cos(k_sy)}{k_{rs}^2 - k^2}\frac{k_{\mathrm{e}}\left(-1^r e^{jk_{\mathrm{e}}a} - 1\right)}{k_r^2 - k_{\mathrm{e}}^2}.$$
(28)

The wavenumbers of the acoustic modes and their weighting by means of volume integration can be written as

$$k_{rs} = \sqrt{k_r^2 + k_s^2}, \ k_r = \frac{r\pi}{a}, \ k_s = \frac{s\pi}{b}, \tag{29}$$

$$\varepsilon_r = \begin{cases} 1, r = 0 \\ 2, r > 0 \end{cases}, \ \varepsilon_s = \begin{cases} 1, s = 0 \\ 2, s > 0 \end{cases}. \tag{30}$$

A. Resolution of evanescent waves

The resolution limits cannot be described mathematically by considering the resonance term or the excitation term in Eq. (28) separately. However, this information is essential because the amplitude decay of acoustic waves in the direction from Π to Ω limits their reconstruction accuracy on the boundary. In the presented example, an evanescent-like decay from boundaries in the k_x (index r) and k_y (index s) directions results from the summation of cosine terms with alternating sign and wavelengths larger than k. The alternating property together with the reactive contribution of modes excited to forced vibration outside their resonance range determines the modal participation as well as the evanescent-like behavior in FIG. 3. The decay takes place in the wavenumber domain $k_{rs} > k_e > k$. The corresponding modes interfere destructively in Ω, whereby the acoustic energy is stored close to the bottom boundary (see FIG. 4).
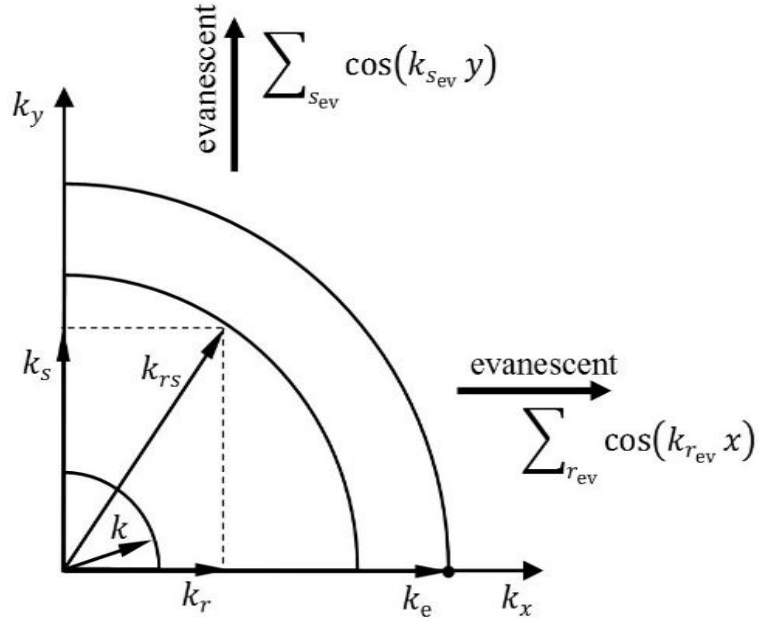
FIG. 3. Schematic of wavenumber domains in $k_x - k_y$ plane: radiation circle (radius k), modal wavenumber (radius k_{rs}), and excitation circle (radius k_e). Destructive interference of acoustic modes (indicated with r_{ev} and s_{ev}) dominates the region outside the excitation circle when $k_{rs} > k_e > k$.

In FIG. 4, the resulting pressure field in the complete volume results from Eq. (28) with $k_e = 2.5k$. It is drawn in the upper sub-figure, comprising the bottom propagative and decaying parts. The dashed line denotes the transition from super resolution of evanescent waves to blurred data in the hologram plane. With no additional random error, the distance of the transition line from the bottom boundary (hereinafter referred to as the "radiation distance") theoretically becomes b, since even very small pressure amplitudes can be detected.
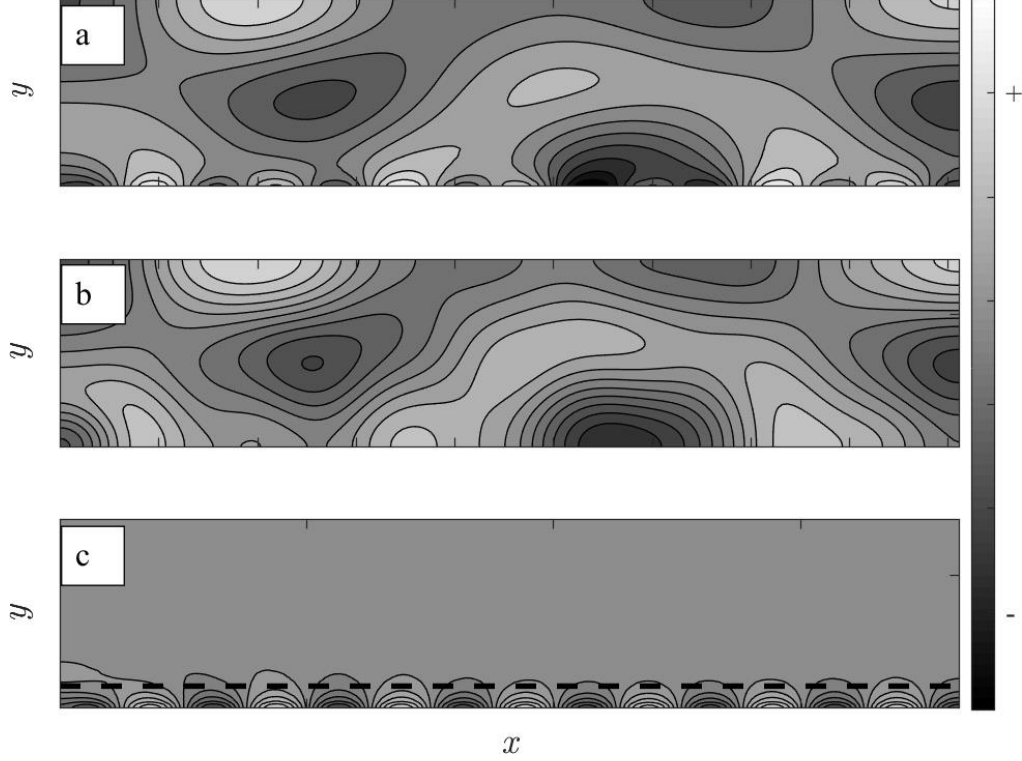
FIG. 4. Real part in [Pa] of the normalized (a) total pressure field in a rigid two-dimensional (2D) rectangular cavity with velocity excitation on the bottom boundary ($k_\mathrm{e} = 2.5k$). The lower sub-figures represent the (b) propagative ($k_{rs} < k$) and (c) evanescent ($k_{rs} > k_\mathrm{e}$) fractions of the upper figure. The radiation distance is marked by the distance between the dashed line and the bottom boundary.

In realistic applications, the measurement precision is limited by the dynamic range (DNR) of the measurement system, which is defined as the logarithmic value of the ratio of the maximum sound pressure $|p|_\mathrm{max}$ to the minimum sound pressure $|p|_\mathrm{min}$ in Ω. With complete cancellation of modes below $|p|_\mathrm{min}$, the connection between the pressure field at receiver points and acoustic sinks and sources on the boundary can be disturbed. This situation appears if an evanescent pressure field falls under the noise floor, depending on the DNR, before reaching the hologram plane. Thus, the radiation distance of inhomogeneous waves from the boundary Π to the field Ω occurs in the sum

of waves $k_{r_{ev}}$ and $k_{s_{ev}}$. A shortfall of the mean sound pressure amplitude along the dashed line in the x direction in FIG. 4 under

$$|p|_{min} = \frac{|p|_{max}}{10^{\frac{DNR}{20}}} \tag{31}$$

is defined as the threshold for detecting the radiation distance from the boundary in FIG. 5. Results for three DNR values with a decreasing noise floor from 20 dB to 40 dB are depicted. It becomes clear that excited waves with wavelengths around the radiation circle propagate through the entire cavity, whereas with increasing spatial frequency of the excitation, destructive interference takes place that causes evanescent-like parts of the pressure field to fall below the noise floor $|p|_{min}$. Thus, with a high noise floor the radiation distance decreases. This in turn leads to blurred input data, with much adverse impact on the ill-posed problem.
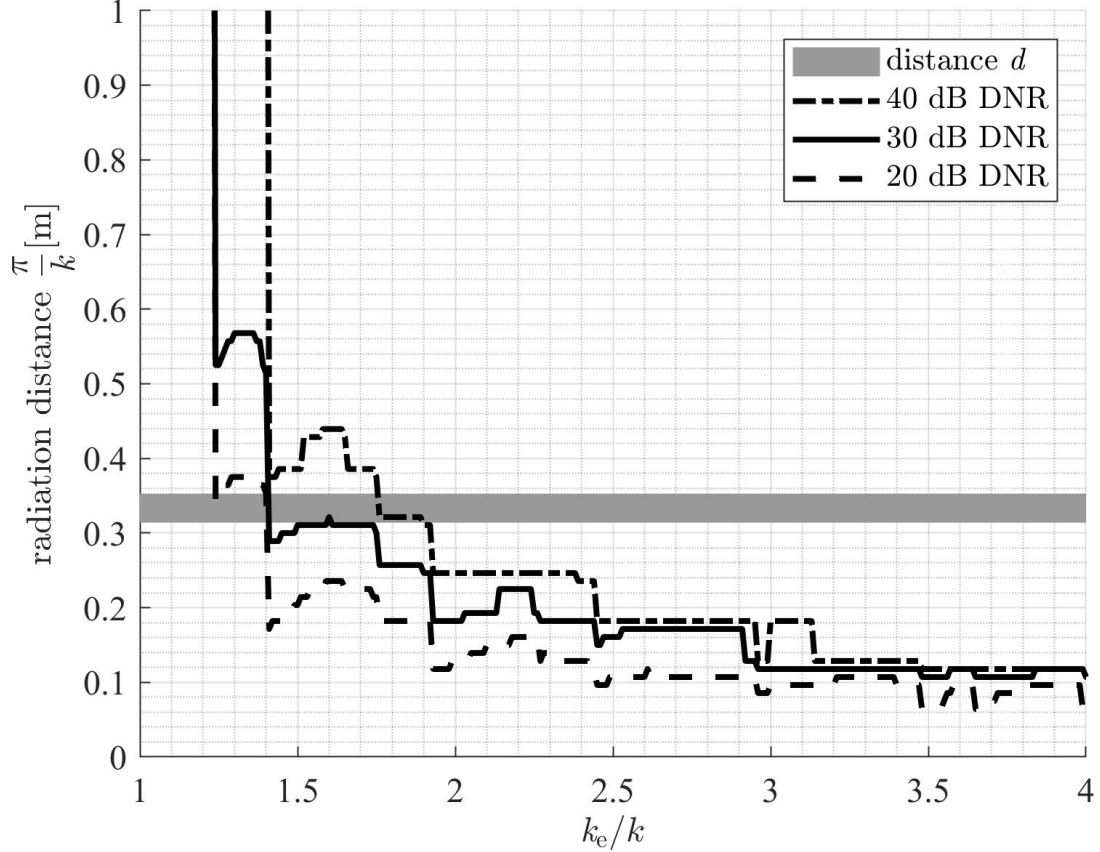
FIG. 5. Radiation distance of evanescent-like waves with respect to the dynamic range (DNR). From the point at which the radiation distance falls below the simulated noise floor, the wavenumber spectra of the pressure field can be detected only partially, thereby leading to blurred reconstruction input data.

Equation (11) contains the ill-posedness represented by small singular values belonging to evanescent waves. FIG. 6 shows the first singular values σ_w ($w = 1,2,\ldots,30$) on the main diagonal of $\boldsymbol{\Sigma}$. Boundary points on the bottom boundary ($y = 0, x$) and all measurement points in Ω are involved in the acoustic transfer matrix. Performing a Fourier transform on the columns w in $\mathbf{U}$ and $\mathbf{V}^H$ extracts the wavenumbers k_u and k_v in singular vectors. The columns contain the basis vectors (modes). It is noteworthy that the most-weighted first seven singular values belong to supersonic singular modes. Thus, large singular values correspond to the contribution of modes

with wavenumbers just below the radiation circle. The direct problem formulation is well-posed because the influence of high spatial frequencies is attenuated by small weights σ_w. The opposite applies to inverse problems in which the reciprocals of small singular values in FIG. 6 dominate the inverse solution. Here, inhomogeneous excitation ($k_e > k$) on the boundary undergoes a rapid decay in the pressure field. Depending on the measurement precision, these waves are only partially detectable and thus generate erroneous results because of amplification of imprecise input data.
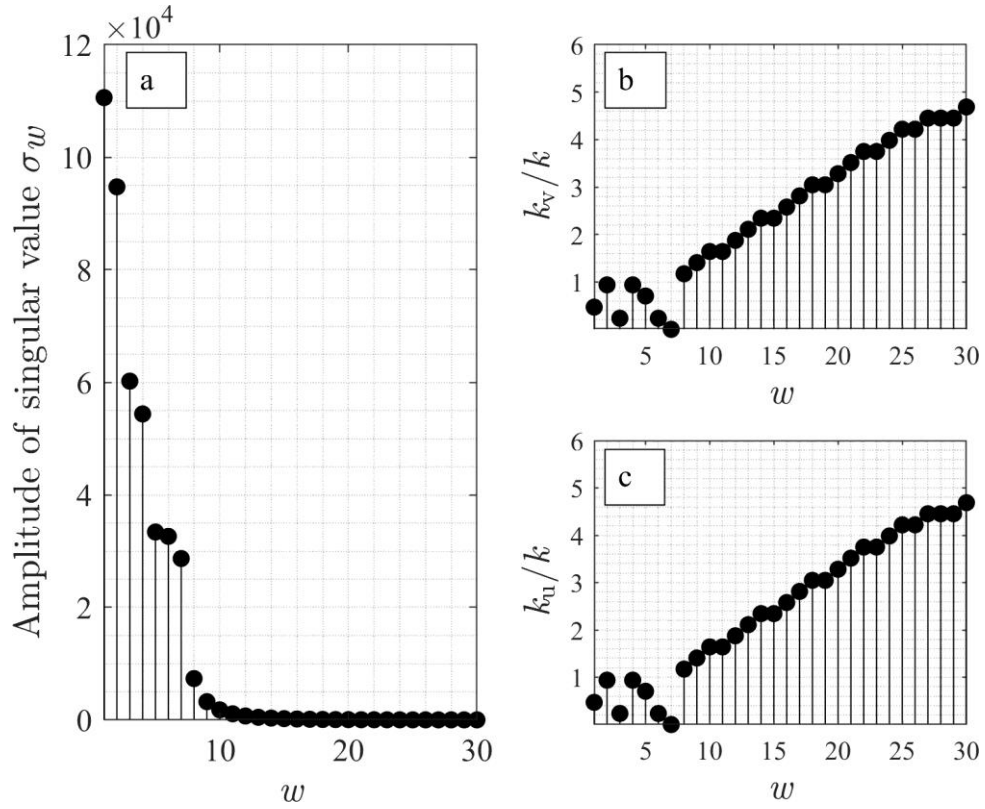

FIG. 6. (a) Amplitudes of first 30 singular values of acoustic transfer matrix from bottom boundary to measurement region in a rigid 2D rectangular cavity. Wavenumbers (k_u, k_v) of corresponding singular vectors in (b) and (c) result from discrete Fourier-transform of columns in $\mathbf{U}$ and $\mathbf{V}^H$. The first seven supersonic singular modes are the most-weighted. An inverse solution is sensitive to the reciprocal of small singular values ($w > 15$) in combination with imprecise input data.

A. Reconstruction error in relation to wavenumber spectra and perturbed input data

Tikhonov regularization leads to a smooth solution of the ill-posed system of linear equations in Eq. (12), which is divided by the patch size h to obtain particle velocities (in units of meters per second) on plane diaphragms. The regularization parameter is from Eq. (13) and minimizes the error norm between the given excitation function and the inverse solution. Furthermore, this procedure ensures comparable solutions. However, an additional random error with Gaussian distribution and zero mean is added to the real and imaginary parts of each discrete sound pressure value in the hologram plane Ω. The associated standard deviation is given by $|p|_{\max}/30$. This statistical assumption approximates a DNR of 30 dB of a hypothetical measurement system.

The reconstruction error in FIG. 7 results from Eq. (13) with inserted optimal regularization parameter μ^{o} in a Monte-Carlo simulation with 100 repetitions. It is divided into three regions. In the first region ($k_{\mathrm{e}}/k < 1$), there is a highly resolved inverse solution above $k_{rs}/k = 1$ because no evanescent waves occur near the radiation circle. In the region below $k_{rs}/k = 1$, the modal wavenumbers do not fully comprise the excitation wavenumber. The second region ($1 \leq k_{\mathrm{e}}/k < 2$) is a transition zone in which the number of evanescent waves increases and the results depend strongly on the modal wavenumber spectrum. The necessary modal spectrum for reconstructing particle velocities on boundaries should comprise twice the excitation wavelength. In the third region ($2 \leq k_{\mathrm{e}}/k \leq 3$), the physical limitation due to the finite sampling distance d in combination with a vanishing radiation distance of evanescent waves in FIG. 5 leads to blurred results, regardless of the wavenumbers involved in the reconstruction process. These results suggest measuring as close as possible to the radiating boundary while keeping the modal wavenumber high enough to take full advantage of the resolution of physical sensors in realistic applications.
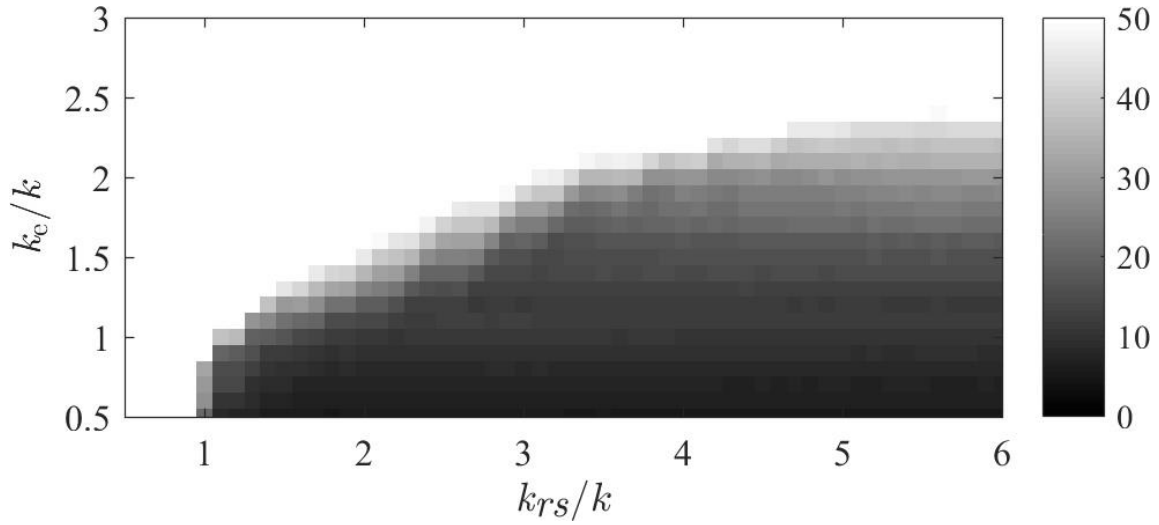
FIG. 7. Reconstruction error in [%] between the given and the reconstructed particle velocity at the bottom boundary according to Eq. (13) with a DNR of 30 dB represented by a random error with Gaussian distribution added to the pressure field. No interpolation is used because each square represents the mean of 100 simulation runs for one wavenumber set.

FIG. 8. Photograph of the fuselage interior with a microphone measurement frame in the back, wooden floor panels on the ground and rubber mats covering the central wing box. The sector of measurements with the LDV is cross-hatched.

IV. EXPERIMENTS

The experimental setup shown in FIG. 8 is an Airbus A400M fuselage with a total length of 30 m and that is suspended freely using pendulum supports. All the response measurements were performed at the Helmut Schmidt University/University of the Federal Armed Forces Hamburg. The measurement setup for the full-scale fuselage is shown schematically in FIG. 9. It is closed by a loading ramp at one end and is open in the flight direction. At the open side, the boundary condition of an acoustically hard wall is approximated by a rigid metal wall with a sound absorber encircling the fuselage front. The gap between the absorber and the skin is 3 cm. Wooden plates cover the floor of the cylindrical structure. The interior sound pressures were measured using an automated scanning robot. Minimizing the influences of evanescent-like waves, 93 microphones

were fixed on the moveable frame, with the distance to the fuselage skin bounded by the frame height. A 10 cm spacing between microphones at a conformal distance of 30–50 cm to the aircraft skin provided response data with high spatial sampling. Sound pressure slices were measured down 14 m of the fuselage interior with a robot step size in the x direction of 10 cm. There was a microphone gap in the lower right corner to permit entry to the back of the frame. Loudspeakers outside the fuselage generated the acoustic excitation. The structural velocities were measured at the upper half inside the cylindrical skin section over a length of 6 m with an out-of-plane LDV that was decoupled from the vibrating structure by foam absorber pads. All the measured Fourier spectra were normalized by the excitation signal spectrum, and the normalization procedure used the same reference signal as the sound pressure measurements.
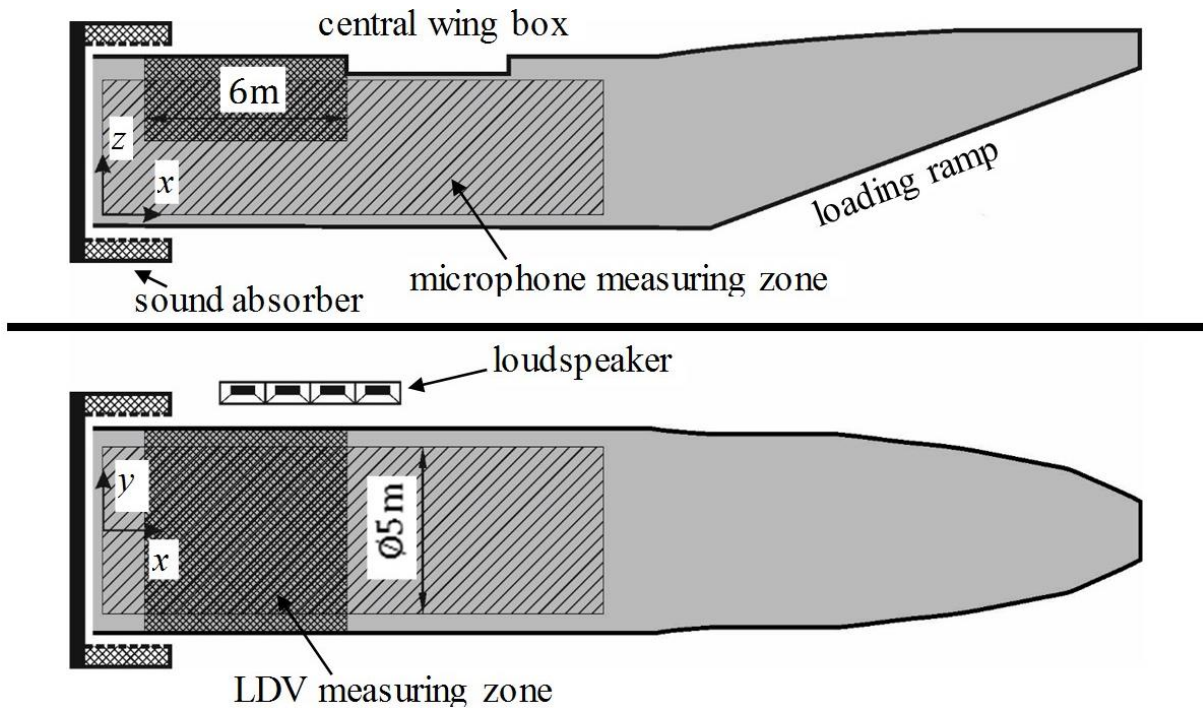

FIG. 9. Schematic of measurement work spaces in Airbus A400M fuselage. A conformal microphone ring frame consisting of 93 microphones was moved automatically to measure the response due to the acoustic excitation. A rotatable laser Doppler vibrometer (LDV) measured the

response of the out-of-plane structural velocity to the excitation signal of loud speakers in the upper half of the cylindrical structure.

A. Numerical implementation of inverse problem

The sum of the contribution of infinite standing-wave modes of the fuselage cavity represents a general solution to the finite sound field subjected to velocity boundary conditions. However, the underlying mathematical model must be as simple as possible. The objective is to eliminate unnecessary details such as ribs and stiffeners. Because of the irregular shape of the cavity, the modal properties cannot be determined in closed form by an analytical solution with geometries for which the wave equation is separable.[35] This problem can be tackled using the numerical technique described in Section II-C. Nevertheless, that approach demands the computation of pairs of eigenvalues and eigenvectors for a 3D model with many degrees of freedom. A simplification is proposed whereby the Neumann problem is formulated by rigid-wall modes of a constantly extruded cross section.[52] The length is chosen arbitrarily as $L = 20$ m, which is larger than the microphone measurement zone in FIG. 9. In this practical example, separating the numerical and analytical acoustic modes leads to a reduced model based on a 2D eigenvalue problem. The resulting cavity model in FIG. 10 is discretized into triangular elements with three nodes and an element edge length of $\bar{h} = \pi/6k$; it contains no ribs or stiffeners. Isoparametric linear functions interpolate the geometric and acoustical quantities. In Fig. 10, the squares are reconstruction points on the boundary, and the diamonds indicate where a microphone was placed on the moveable frame. Because the modal characteristics in the axial direction are assumed to be known (rigid wall), the eigenvalue problem is reduced to a one-dimensional (1D) and a 2D acoustically hard-walled system model connected in series.
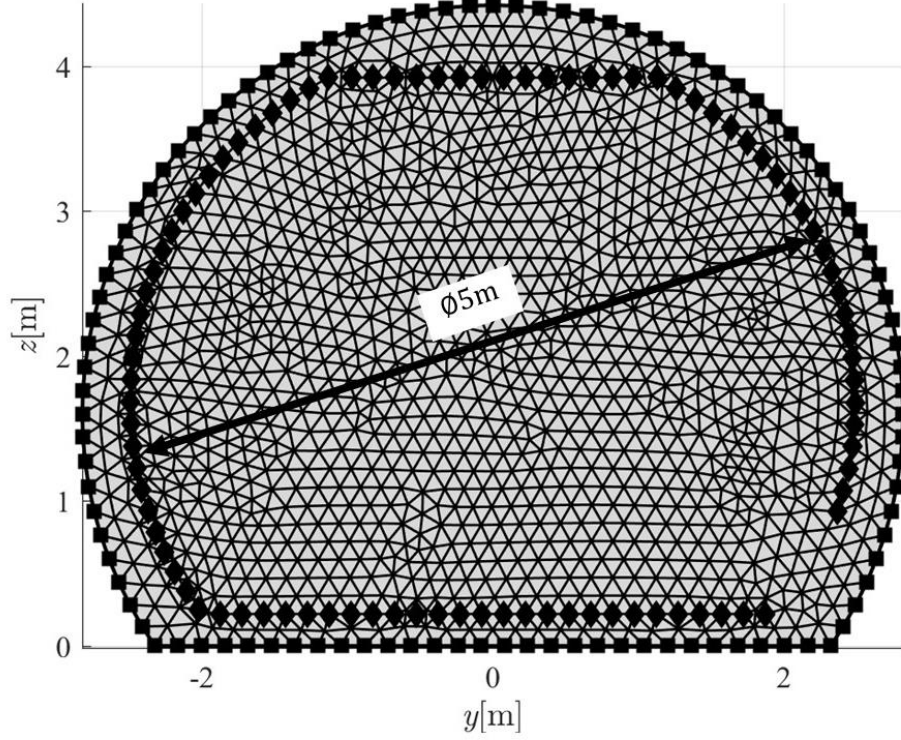
25

FIG. 10. Finite element mesh of 2D simplified cavity model of experimental setup. Diamonds mark microphone positions. Squares coincide with positions on the floor panels and on the fuselage skin where the velocity is reconstructed. The model ignores irregularities such as ribs and stiffeners.

Pre-sorted sets of eigenvalues and eigenvectors are used to combine both models into a 3D model. From Eq. (22), the angular eigenfrequencies $\bar{\omega}^{2D}$ of the 2D model on the main diagonal of $\mathbf{\Omega}^{2D}$ are given by

$$\mathbf{\Omega}^{2D} = \sqrt{\mathbf{\Psi}^{2D^{T}} \mathbf{K}^{2D} \mathbf{\Psi}^{2D}}, \tag{32}$$

where $\mathbf{K}^{2D}$ and $\mathbf{\Psi}^{2D}$ are the stiffness matrix and the projection matrix, respectively, of the 2D model in FIG. 10. The wavenumber eigenvalues of the 3D model are given by

$$\bar{k}_n = \sqrt{\frac{(\bar{\omega}_l^{2D})^2}{c^2} + \left(\frac{m\pi}{L}\right)^2}. \tag{33}$$

Double indices are mapped comprising the lth angular eigenfrequency and the mth analytical eigenvalue of a 1D standing wave onto the single index n to get the eigenvalues in ascending order, namely $0 \leq \bar{k}_1(l,m) \leq \bar{k}_2(l,m) \leq \cdots \leq \bar{k}_n(l,m)$. With Eq. (33), the 2D eigenvalue problem is solved once for the mesh in FIG. 10 with an element length of $\bar{h} = \pi/6k_{\mathrm{max}}$ corresponding to the highest analyzed frequency of 140 Hz. Each eigenvalue leads to a vanishing determinant of the undamped impedance matrix connected to the 3D model. It is paired with its corresponding eigenvector $\boldsymbol{\psi}_n \in \mathbb{R}^{1 \times D(L/\bar{h})}$ by

$$\boldsymbol{\psi}_n = \boldsymbol{\Psi}_l^{2\mathrm{D}} \cos\left(\frac{m\pi\bar{\mathbf{x}}}{L}\right). \tag{34}$$

It is known from Eq. (18) that $\boldsymbol{\Psi}^{2\mathrm{D}}$ has dimensions $D \times E$, where D is the total number of degrees of freedom in the 2D finite element model in FIG. 10 and E is the number of eigensolutions involved in the inverse calculation. The vector $\bar{\mathbf{x}} \in \mathbb{R}^{L/\bar{h} \times 1}$ contains the sampled coordinates in the axial direction of the 3D model between zero and L. The length of the $L/\bar{h}$ entries matches the element size of the 2D finite element mesh to obtain a regularly spaced discretization. The index l picks the lth column (eigenvector) in $\boldsymbol{\Psi}$, in the same manner as in Eq. (33), to obtain pairs of eigenvalues $\bar{k}_n$ and eigenvectors $\boldsymbol{\psi}_n \in \mathbb{R}^{1 \times D(L/\bar{h})}$ of the 3D model in ascending order. Selecting the boundary nodes and measurement nodes gives the transfer matrix according to Eq. (26):

$$\tilde{\mathbf{Z}} = -\mathrm{j}\omega\varrho \sum_{n=1}^{E} \frac{\varepsilon_n}{L} \frac{\widehat{\boldsymbol{\psi}}_n \widecheck{\boldsymbol{\psi}}_n^T}{\left(\bar{k}_n^2 - k^2\right)}. \tag{35}$$

The normalization factor ε_n for the cosine function appears to be 1 for the mode with a zero axial wavenumber and 2 for all other modes. With Eqs. (10)–(12), a solution to the inverse problem is obtained.

B. Reconstruction of structural velocity

FIG. 11 depicts the spatially distributed amplitude of the reconstructed particle velocities together with the amplitude of the structural velocities measured with the LDV. The boundary is divided into patches of length $\pi/6k$ to decrease the computation time because the SVD leads to lengthy numerical computations for a large number of degrees of freedom. This leads to different spatial resolutions for the reconstructed velocities, where the resolution of the measurement grid is adapted to the reconstruction points. The results for the three selected frequencies agree well. A decrease of the reconstruction error with an increasing modal wavelength is noticeable. The experimental results are consistent with the findings for the transition zone using the simplified numerical example in FIG. 7.
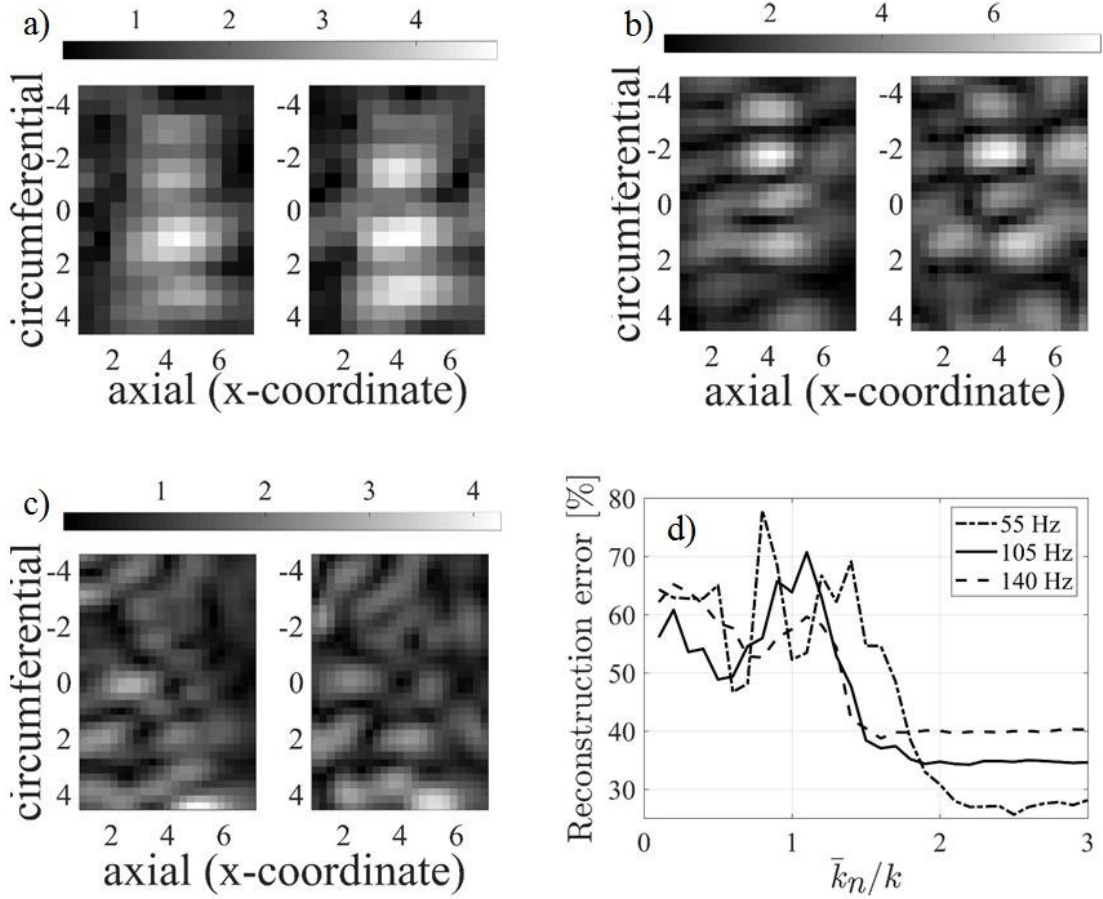
FIG. 11. Unwrapped image plot (colorbar in units of $(m/Vs)10^{-3}$) of measured (with LDV) and reconstructed structural velocity amplitude for (a) 55 Hz, (b) 105 Hz, and (c) 140 Hz in the LDV measurement workspace. In each sub-figure, the measured results are displayed on the left and the reconstructed results are shown on the right (all values on the axes in image plots are in meters). The maximum modal wavenumber is three times the acoustic wavenumber $(\bar{k}_n/k = 3)$. The resolution of the evaluation points depends on the considered frequency. Sub-figure (d) depicts the reconstruction error over the maximum modal wave number in the acoustic transfer matrix.

V. CONCLUSIONS

With the objective of reconstructing inversely the active sources of sound in an interior domain due to structural vibrations, the numerical implementation of the modal approach via FEM was

extended to NAH. The approach adopted in this study relates sound pressure measurements in a cavity to the normal particle velocities on its boundary. It was applied first in closed-form solution to a simple 2D room model. The analysis revealed the dependency of the resolution of the backward projection on the dynamic range as well as on the ability to detect evanescent-like waves near radiating boundaries. These findings are identical with those known from classical NAH. Within this example, the modal spectrum necessary for reconstructing particle velocities on boundaries should comprise twice the excitation wavelength.

An experimental application of the FEM-based NAH to the reconstruction of the velocity field in a highly reverberant full-scale fuselage was realized. The required acoustic transfer functions resulted from a linear approximation of the acoustic environment with finite elements utilizing a 2D model with a constant cross section. The focus here was on an acceptable model reduction ensuring a sufficient resolution of the reconstructed velocity fields. It was found that the wavenumber spectra in the computed frequency response function can have a large influence on the reconstruction results. A ratio of the modal wave number to the acoustic wavenumber of at least two leads to satisfactory results. However, partially measured structural velocities might be unavailable in a different scenario. Therefore, different parameter-choice methods must be evaluated. Furthermore, because no large axial dependency is expected for the occurring structural and acoustic wavelengths, the optimal regularization parameter that is obtained can be used to calculate sound-field quantities where there are no comparative results from LDV measurements.

ACKNOWLEDGMENTS

[1] E. G. Williams, J. D. Maynard, and E. Skudrzyk, "Sound source reconstructions using a microphone array," J. Acoust. Soc. Am. **68**, 340–344 (1980).

[2] J. Hald, "Basic theory and properties of statistically optimized near-field acoustical holography," J. Acoust. Soc. Am. **125**, 2105–2120 (2009).

[3] J. R. Shewell and E. Wolf, "Inverse diffraction and a new reciprocity theorem," J. Opt. Soc. Am. **58**, 1596–1603 (1968).

[4] T. Loyau, J.-C. Pascal, and P. Gaillard, "Broadband acoustic holography reconstruction from acoustic intensity measurements. I: Principle of the method," J. Acoust. Soc. Am. **84**, 1744–1750 (1988).

[5] E. Fernandez-Grande, F. Jacobsen, and Q. Leclère, "Sound field separation with sound pressure and particle velocity measurements," J. Acoust. Soc. Am. **132**, 3818–3825 (2012).

[6] D. L. Hallmann, J. S. Bolton, S. M. Dumbacher, D. L. Brown, B. W. Libbey, and M. J. Lally, "Acoustic source location in vehicle cabins and free-field with nearfield acoustical holography via acoustic arrays," in *Proceedings of the 19th International Seminar of Modal Analysis, Leuven, Belgium*, Vol. 2 (1994), pp. 841–851.

[7] M. Villot, G. Chavériat, and J. Roland, "Phonoscopy: An acoustical holography technique for plane structures radiating in enclosed spaces," J. Acoust. Soc. Am. **91**, 187–195 (1992).

[8] R. Visser, "A boundary element approach to acoustic radiation and source identification," Ph.D. dissertation, University of Twente, Enschede, 2004.

[9]B.-K. Kim and J.-G. Ih, "On the reconstruction of the vibro-acoustic field over the surface enclosing an interior space using the boundary element method," J. Acoust. Soc. Am. **100**, 3003–3016 (1996).

[10]N. P. Valdivia and E. G. Williams, "Study of the comparison of the methods of equivalent sources and boundary element methods for near-field acoustic holography," J. Acoust. Soc. Am. **120**, 3694–3705 (2006).

[11]E. G. Williams, B. H. Houston, P. C. Herdic, S. T. Raveendra, and B. Gardner, "Interior near-field acoustical holography in flight," J. Acoust. Soc. Am. **108**, 1451–1463 (2000).

[12]L. Cremer, "Synthesis of the sound field of an arbitrary rigid radiator in air with arbitrary particle velocity distribution by means of spherical sound fields," Acustica **55**, 44-46 (1984).

[13]G. H. Koopmann, L. Song, and J. B. Fahnline, "A method for computing acoustic fields based on the principle of wave superposition," J. Acoust. Soc. Am. **86**, 2433–2438 (1989).

[14]M. Gensane and F. Santon, "Prediction of sound fields in rooms of arbitrary shape: Validity of the image sources method," J. Sound Vib. **63**, 97–108 (1979).

[15]M. E. Johnson, S. J. Elliott, K.-H. Baek, and J. Garcia-Bonito, "An equivalent source technique for calculating the sound field inside an enclosure containing scattering objects," J. Acoust. Soc. Am. **104**, 1221–1231 (1998).

[16]S. F. Wu and J. Yu, "Reconstructing interior acoustic pressure fields via Helmholtz equation least-squares method," J. Acoust. Soc. Am. **104**, 2054–2060 (1998).

[17]C.-X. Bi, D.-Y. Hu, Y.-B. Zhang, and W.-Q. Jing, "Identification of active sources inside cavities using the equivalent source method-based free-field recovery technique," J. Sound Vib. **346**, 153–164 (2015).

[18]M. R. Bai, C.-C. Chen, and J.-H. Lin, "On optimal retreat distance for the equivalent source method-based nearfield acoustical holography," J. Acoust. Soc. Am. **129**, 1407–1416 (2011).

[19] I.-Y. Jeon and J.-G. Ih, "On the holographic reconstruction of vibroacoustic fields using equivalent sources and inverse boundary element method," J. Acoust. Soc. Am. **118**, 3473–3482 (2005).

[20] P. A. Nelson and S. H. Yoon, "Estimation of acoustic source strength by inverse methods: part I, conditioning of the inverse problem," J. Sound Vib. **233**, 639–664 (2000).

[21] W. Jung, S. J. Elliott, and J. Cheer, "Identifying of interior noise sources in a vehicle cabin using the inverse method," in *Proceedings of the 23rd International Congress on Sound and Vibration, Athens, Greece* (2016), pp. 4235–4242.

[22] J. M. Mason and F. J. Fahy, "Development of a reciprocity technique for the prediction of propeller noise transmission through aircraft fuselages," Noise Control Eng. J. **34**, 43–52 (1990).

[23] E. G. Williams, "Regularization methods for near-field acoustical holography," J. Acoust. Soc. Am. **110**, 1976–1988 (2001).

[24] A. Roger, D. Maystre, and M. Cadilhac, "On a problem of inverse scattering in optics: the dielectric inhomogeneous medium," J. Opt. **9**, 83–89 (1978).

[25] K. Chelliah, G. G. Raman, and R. T. Muehleisen, "Enhanced nearfield acoustic holography for larger distances of reconstructions using fixed parameter Tikhonov regularization," J. Acoust. Soc. Am. **140**, 114–120 (2016).

[26] J. Cullum, "The effective choice of the smoothing norm in regularization," Math. Comp. **33**, 149–170 (1979).

[27] P. C. Hansen, *Rank-Deficient and Discrete Ill-Posed Problems* (Society for Industrial and Applied Mathematics, Philadelphia, 1998), Chap. 7, pp. 175-192.

[28] F. Pockels, *Über die partielle Differentialgleichung ($\Delta u+k^2 u$)=0 und deren Auftreten in der mathematischen Physik (On the Partial Differential Equation ($\Delta u+k^2 u$)=0 and their Occurrence in Mathematical Physics)* (Teubner, Leipzig, 1891), Chap. 4, pp. 280-317.

[29]P. M. Morse, *Vibration and Sound* (MacGraw-Hill, New York, 1948), Chap. 8, pp. 413-431.

[30]P. M. Morse and H. Feshbach, *Methods of Theoretical Physics* (McGraw-Hill, New York, 1953), Chap. 7, pp. 791-895.

[31]M. R. Schroeder and K. H. Kuttruff, "On frequency response curves in rooms. Comparison of experimental, theoretical, and Monte Carlo results for the average frequency spacing between maxima," J. Acoust. Soc. Am. **34**, 76–80 (1962).

[32]P. M. Morse and K. U. Ingard, *Theoretical Acoustics* (Princeton University Press, Princeton, 1986), Chap. 9, pp. 554-575.

[33]R. J. Alfredson, "A note on the use of the finite difference method for predicting steady state sound fields," Acustica **28**, 296–301 (1973).

[34]P. Filippi, *Theoretical Acoustics and Numerical Techniques* (Springer, Vienna, 1983), Chap. 2, pp. 51-104.

[35]E. G. Williams, "On Green's functions for a cylindrical cavity," J. Acoust. Soc. Am. **102**, 3300–3307 (1997).

[36]R. Anderssohn, S. Marburg, and C. Großmann, "FEM-based reconstruction of sound pressure field damped by partially absorbing boundary conditions," Mech. Res. Comm. **33**, 851–859 (2006).

[37]J. Drenckhan, I. Schäfer, and D. Sachau, "Identification of noise sources in an aircraft cabin," in *Proceedings of the International Modal Analysis Conference XXII, Dearborn, Michigan* (2004), Paper No. 226.

[38]T. Kletschkowski, M. Weber, and D. Sachau, "Identification of noise sources in an aircraft fuselage using an inverse method based on a finite element model," Acta Acustica united with Acustica **97**, 974–983 (2011).

[39]M. Kaltenbacher, B. Kaltenbacher, and S. Gombots, "Inverse scheme for acoustic source localization using microphone measurements and finite element simulations," Acta Acustica united with Acustica **104**, 647–656 (2018).

[40]K.-J. Bathe, *Finite Element Procedures* (Prentice-Hall, New Jersey, 1996), Chap. 9, pp. 785-800.

[41]M. Aucejo, N. Totaro, and J.-L. Guyader, "Identification of source velocities with inverse patch transfer functions method," J. Acoust. Soc. Am. **123**, 3310 (2008).

[42]S. Forget, N. Totaro, J. L. Guyader, and M. Schaeffer, "Source fields reconstruction with 3d mapping by means of the virtual acoustic volume concept," J. Sound Vib. **381**, 48–64 (2016).

[43]R. Anderssohn and S. Marburg, "Nonlinear approach to approximate acoustic boundary admittance in cavities," J. Comp. Acous. **15**, 63–79 (2007).

[44]S. Marburg and H.-J. Hardtke, "A study on the acoustic boundary admittance. Determination, results and consequences," Eng. Anal. Bound. Elem. **23**, 737–744 (1999).

[45]D. V. Nehete, S. V. Modak, and K. Gupta, "Experimental studies in finite element model updating of vibro-acoustic cavities using coupled modal data and FRFs," Applied Acoustics **150**, 113–123 (2019).

[46]Z. Wan, T. Wang, Q. Huang, and J. Wang, "Acoustic finite element model updating using acoustic frequency response function," Finite Elements in Analysis and Design **87**, 1–9 (2014).

[47]E. G. Williams, *Fourier Acoustics* (Academic Press, San Diego, 1999), Chap. 8, pp. 251-295.

[48]E. H. Dowell, C.-F. Chao, and D. B. Bliss, "Absorption material mounted on a moving wall-fluid/wall boundary condition," J. Acoust. Soc. Am. **70**, 244–245 (1981).

[49]S. Marburg, "Normal modes in external acoustics. part I: investigation of the one-dimensional duct problem," Acta Acustica united with Acustica **91**, 1063–1078 (2005).

[50]Q. Leclère, A. Pereira, C. Bailly, J. Antoni, and C. Picard, "A unified formalism for acoustic imaging based on microphone array measurements," Int. J. Aeroacoust. **16**, 431–456 (2017).

[51]M. Petyt, *Introduction to Finite Element Vibration Analysis* (Cambridge University Press, Cambridge, 2010), Chap. 12, pp. 357-412.

[52]L. D. Pope, E. G. Wilby, and J. F. Wilby, "Propeller aircraft interior noise model, part I: Analytical model," J. Sound Vib. **118**, 449–467 (1987).